Supplement of Solid Earth, 13, 745–759, 2022
https://doi.org/10.5194/se-13-745-2022-supplement

Solid Earth
Open Access

Supplement of

Thermal equation of state of the main minerals of eclogite: Constraining the density evolution of eclogite during the delamination process in Tibet

Zhilin Ye et al.

Correspondence to: Dawei Fan (fandawei@vip.gyig.ac.cn) and Jingui Xu (xujingui@hawaii.edu)

Text S1-S3
Table S1-S3
Figure S1-S13

Text S1. Discussion on the effects of bulk modulus and its pressure derivate of minerals on density

To evaluate the effect of bulk modulus (K_{T0}) and its pressure derivate (K_{T0}'), we calculate the mineral density using K_{T0} and K_{T0}' in different experiments (Figure S4). The results show that the influence of K_{T0} on density is limited. Only when the ΔK_{T0} between the two experiments (Arimoto et al., 2015; Xu et al., 2019) is 20 GPa, the density difference of 0.27% will be generated at 140 km (~4.2 GPa) (Fig. S5). Moreover, the results of density differences in this study are comparable to that of Milani et al. (2015). For omphacite, the density profiles from Xu et al. (2019) and Zhang et al. (2016) are the same, as well as the results of this study and Nishihara et al. (2003). In this case, the maximum density difference is only 0.3%. But for epidote, due to too large K_{T0} (~162 GPa) in Holland et al. (1996) experiment, the maximum density difference is ~0.6%-1.2%. The density results of epidote in this study are similar to those of Qin et al. (2016) and Gatta et al. (2011). The influence of K_{T0}' on density is limited, and only the values of K_{T0} with very large differences can have a conspicuous impact on density. Meanwhile, the influence of K_{T0} and K_{T0}' on mineral density is interactive.

Text S2. Density profile along Cenozoic geothermal line

The density profiles of eclogite and peridotite along the Cenozoic geotherm are shown in Figure 6b. With an increase of 10 vol. % garnet, the density of eclogite increases by ~1.8%. The density of Tibetan eclogite in this study is 3.45-3.58 g/cm^3, which is approximately 6.9%-10.8% larger than that of the surrounding peridotite (3.23 g/cm^3) at ~60 km. The densities of eclogite increase by ~2.0% for high-Fe eclogite and ~1.4% for low-Fe eclogite. A comparison of the surrounding peridotite with eclogites of different iron contents eclogite shows that the density of high-Fe eclogite (3.58-3.73 g/cm^3) is 11%-15.5% denser and that of low-Fe eclogite (3.47-3.56 g/cm^3) is 7.3%-10.4% denser.

Text S3. Stokes' Law

The velocity of fragmented block is calculated using the Stockes'equation,

$$\eta = \frac{2\mathrm{r}^2 g\left(\rho - \rho_0\right)}{9\upsilon} \tag{1}$$

where
η = absolute viscosity (poise)
r = radius of fragmented block (cm)
g = acceleration of fragmented block (cm·s^{-2})
ρ = density of fragmented block (g·cm^{-3})
ρ_0 = density of surrounding lithospheric mantle (g·cm^{-3})
ν = terminal velocity of fragmented block in surrounding lithospheric mantle (cm·s^{-2})

Table S1. Unit-cell parameters of garnet, omphacite, epidote at high pressures and high temperatures.

(a) Garnet

P (GPa)	*T* (K)	*a* (Å)	*V* (Å^3)
0.0001	300	11.612(2)	1565.8(4)
0.45(2)	300	11.602(1)	1561.6(3)
1.20(2)	300	11.589(1)	1556.5(2)
2.45(2)	300	11.560(1)	1545.0(2)
3.47(2)	300	11.537(1)	1535.4(1)
4.55(2)	300	11.515(1)	1526.8(2)
6.10(2)	300	11.483(1)	1514.2(2)
8.00(2)	300	11.445(1)	1499.3(3)
9.95(2)	300	11.409(1)	1485.2(1)
11.97(2)	300	11.371(1)	1470.1(4)
16.65(2)	300	11.294(1)	1440.6(2)
18.70(2)	300	11.261(2)	1427.8(4)
1.75(2)	400	11.586(1)	1555.4(1)
2.70(2)	400	11.566(1)	1547.1(1)
2.90(2)	400	11.559(1)	1544.3(2)
3.97(2)	400	11.536(1)	1535.0(2)
5.40(2)	400	11.507(1)	1523.8(1)
7.10(2)	400	11.475(1)	1510.6(1)
9.15(2)	400	11.433(1)	1494.5(1)
13.47(2)	400	11.354(1)	1463.7(1)
17.25(2)	400	11.291(1)	1439.6(2)
19.90(2)	400	11.249(2)	1423.6(4)
2.30(2)	500	11.585(1)	1554.8(2)
3.45(2)	500	11.556(1)	1543.3(2)
4.47(2)	500	11.535(1)	1534.9(1)
6.37(2)	500	11.499(1)	1520.6(2)
8.07(2)	500	11.467(1)	1507.7(1)
10.30(2)	500	11.424(1)	1490.8(2)
15.15(2)	500	11.335(1)	1456.4(1)
17.85(2)	500	11.293(1)	1440.3(3)
21.50(2)	500	11.232(1)	1416.9(3)
3.07(2)	600	11.577(1)	1551.7(1)
4.27(2)	600	11.553(1)	1541.8(2)
5.05(2)	600	11.534(1)	1534.5(2)
7.85(2)	600	11.479(1)	1512.5(2)
12.10(2)	600	11.398(1)	1480.7(2)
17.02(2)	600	11.315(1)	1448.6(2)
23.30(2)	600	11.212(1)	1409.3(2)
3.95(2)	700	11.569(1)	1548.3(2)
5.60(2)	700	11.535(1)	1534.6(2)
9.30(2)	700	11.461(1)	1505.4(1)
13.90(2)	700	11.376(1)	1472.3(1)
19.70(2)	700	11.281(1)	1435.1(2)
25.57(2)	700	11.190(1)	1401.2(2)

(b) Omphacite

P (GPa)	T (K)	a (Å)	b (Å)	c (Å)	β (°)	V (Å^3)
0.0001	300	9.593(5)	8.771(8)	5.257(1)	106.83(3)	423.3(4)
0.45(2)	300	9.518(4)	8.737(5)	5.252(2)	105.19(2)	421.5(3)
1.20(2)	300	9.503(3)	8.739(4)	5.239(1)	105.27(2)	419.7(3)
2.45(2)	300	9.488(3)	8.694(4)	5.220(1)	105.39(2)	415.1(3)
3.47(2)	300	9.451(4)	8.694(5)	5.207(1)	106.38(3)	412.6(3)
4.55(2)	300	9.444(4)	8.659(6)	5.193(2)	105.55(1)	409.1(3)
6.10(2)	300	9.443(3)	8.611(19)	5.179(1)	106.18(3)	404.4(9)
8.00(2)	300	9.410(3)	8.563(16)	5.159(1)	106.03(2)	399.5(8)
9.95(2)	300	9.380(6)	8.493(8)	5.135(3)	105.92(5)	393.4(6)
11.97(2)	300	9.345(3)	8.487(5)	5.103(1)	105.99(2)	389.1(3)
16.65(2)	300	9.276(3)	8.384(5)	5.061(1)	105.50(2)	379.3(3)
18.70(2)	300	9.284(4)	8.350(7)	5.040(3)	106.23(4)	375.1(4)
1.75(2)	400	9.490(6)	8.755(8)	5.235(3)	105.26(4)	419.6(5)
2.70(2)	400	9.537(4)	8.723(6)	5.217(4)	106.47(3)	416.2(4)
2.90(2)	400	9.478(3)	8.710(4)	5.217(2)	105.36(2)	415.3(2)
3.97(2)	400	9.450(3)	8.703(4)	5.201(1)	105.52(2)	412.2(2)
5.40(2)	400	9.448(4)	8.628(6)	5.185(2)	105.58(3)	407.1(4)
7.10(2)	400	9.425(3)	8.632(19)	5.172(2)	106.16(3)	404.2(9)
9.15(2)	400	9.390(3)	8.557(16)	5.141(1)	105.94(4)	397.2(8)
13.47(2)	400	9.322(3)	8.497(6)	5.093(2)	106.11(2)	387.6(3)
17.25(2)	400	9.237(3)	8.448(5)	5.057(1)	105.46(1)	379.0(3)
19.90(2)	400	9.212(5)	8.371(7)	5.033(2)	105.41(3)	374.2(4)
2.30(2)	500	9.486(7)	8.770(9)	5.231(3)	105.32(4)	419.7(6)
3.45(2)	500	9.475(3)	8.711(5)	5.214(1)	105.44(3)	414.9(3)
4.47(2)	500	9.481(6)	8.716(9)	5.200(3)	106.37(3)	412.3(6)
6.37(2)	500	9.438(4)	8.614(5)	5.178(2)	105.64(3)	405.5(3)
8.07(2)	500	9.410(4)	8.637(5)	5.158(1)	106.07(2)	402.9(3)
10.30(2)	500	9.378(2)	8.540(12)	5.129(1)	105.81(2)	395.2(6)
15.15(2)	500	9.320(4)	8.458(6)	5.080(2)	106.08(3)	384.8(4)
17.85(2)	500	9.277(3)	8.455(5)	5.056(1)	105.46(2)	380.3(3)
21.50(2)	500	9.254(5)	8.321(8)	5.026(1)	106.27(2)	371.5(5)
3.07(2)	600	9.520(4)	8.790(5)	5.224(1)	106.58(3)	419.0(3)
4.27(2)	600	9.467(4)	8.699(5)	5.211(1)	105.47(2)	415.6(3)
5.05(2)	600	9.483(3)	8.712(4)	5.197(1)	106.33(2)	412.0(3)
7.85(2)	600	9.411(6)	8.632(8)	5.167(2)	105.74(2)	404.0(5)
12.10(2)	600	9.345(4)	8.548(9)	5.116(2)	105.79(2)	393.3(5)
17.02(2)	600	9.301(2)	8.433(4)	5.066(1)	106.13(3)	381.7(2)
23.30(2)	600	9.176(2)	8.339(3)	5.011(1)	105.29(1)	369.2(4)
3.95(2)	700	9.468(3)	8.752(4)	5.218(1)	105.42(3)	416.8(3)
5.60(2)	700	9.480(7)	8.707(9)	5.196(3)	106.33(4)	411.6(6)
9.30(2)	700	9.407(3)	8.622(5)	5.151(1)	106.02(1)	401.5(3)
13.90(2)	700	9.348(4)	8.490(5)	5.104(2)	106.03(2)	389.3(3)
19.70(2)	700	9.241(4)	8.381(6)	5.054(1)	105.40(1)	377.4(3)
25.57(2)	700	9.156(4)	8.289(7)	4.993(2)	105.16(2)	365.7(4)

(c) Epidote

P (GPa)	*T* (K)	*a* (Å)	*b* (Å)	*c* (Å)	*β* (°)	*V* ($Å^3$)
0.0001	300	8.9045(1)	5.6205(3)	10.267(1)	116.18(2)	461.2(2)
0.45(2)	300	8.8918(5)	5.6361(4)	10.147(1)	115.38(3)	459.4(1)
1.20(2)	300	8.8746(5)	5.6258(3)	10.125(1)	115.25(3)	456.7(1)
2.45(2)	300	8.8445(5)	5.6093(3)	10.094(1)	115.32(3)	452.3(1)
3.47(2)	300	8.8211(5)	5.5964(3)	10.066(1)	115.63(3)	448.7(1)
4.55(2)	300	8.7977(5)	5.5857(3)	10.040(1)	115.55(3)	445.2(1)
6.10(2)	300	8.7579(5)	5.5695(3)	9.995(1)	115.42(4)	440.1(1)
8.00(2)	300	8.7170(5)	5.5527(3)	9.950(1)	115.41(4)	434.6(1)
9.95(2)	300	8.6684(4)	5.5025(4)	9.884(1)	115.41(3)	427.8(1)
11.97(2)	300	8.5382(5)	5.5304(3)	9.843(1)	116.19(3)	421.9(1)
16.65(2)	300	8.4567(5)	5.5098(3)	9.747(1)	115.50(3)	409.9(1)
18.70(2)	300	8.4174(5)	5.5016(4)	9.7101(1)	115.83(3)	404.7(1)
1.75(2)	400	8.8694(5)	5.6251(3)	10.123(1)	115.49(3)	456.6(1)
2.70(2)	400	8.8487(5)	5.6121(3)	10.100(1)	115.55(3)	453.3(1)
2.90(2)	400	8.8411(5)	5.6097(3)	10.093(1)	115.37(3)	452.3(1)
3.97(2)	400	8.8168(5)	5.5947(3)	10.061(1)	115.51(3)	448.6(1)
5.40(2)	400	8.7855(5)	5.5818(3)	10.029(1)	115.38(3)	444.3(1)
7.10(2)	400	8.7433(5)	5.5641(3)	9.980(1)	115.35(3)	438.6(1)
9.15(2)	400	8.7108(5)	5.5477(3)	9.933(1)	115.40(3)	431.8(1)
13.47(2)	400	8.5532(4)	5.5312(4)	9.811(1)	115.11(2)	419.2(1)
17.25(2)	400	8.5162(4)	5.5012(4)	9.741(1)	115.74(2)	409.2(1)
19.90(2)	400	8.4062(5)	5.4989(4)	9.696(1)	115.67(3)	402.4(1)
2.30(2)	500	8.8649(5)	5.6276(3)	10.119(1)	115.45(3)	456.7(1)
3.45(2)	500	8.8363(5)	5.6103(3)	10.082(1)	115.34(3)	452.3(1)
4.47(2)	500	8.8130(5)	5.5946(3)	10.055(1)	115.46(3)	448.7(1)
6.37(2)	500	8.7731(5)	5.5759(3)	10.011(1)	115.31(3)	442.7(1)
8.07(2)	500	8.7376(4)	5.5609(3)	9.965(1)	115.17(3)	437.1(1)
10.30(2)	500	8.6902(4)	5.5345(3)	9.913(1)	115.19(3)	429.5(1)
15.15(2)	500	8.5285(4)	5.5214(4)	9.793(1)	115.32(2)	415.7(1)
17.85(2)	500	8.4837(4)	5.5053(4)	9.736(1)	115.23(2)	408.3(1)
21.50(2)	500	8.4076(4)	5.4712(4)	9.667(1)	115.16(2)	399.2(1)
3.07(2)	600	8.8573(5)	5.6185(3)	10.106(1)	115.41(3)	455.4(1)
4.27(2)	600	8.8312(5)	5.6039(3)	10.076(1)	115.35(3)	451.6(1)
5.05(2)	600	8.8092(5)	5.5943(3)	10.053(1)	115.50(3)	447.2(1)
7.85(2)	600	8.7522(5)	5.5652(3)	9.981(1)	115.48(3)	438.9(1)
12.10(2)	600	8.5689(5)	5.5383(3)	9.880(1)	116.07(3)	425.4(1)
17.02(2)	600	8.4718(5)	5.5144(3)	9.768(1)	115.81(3)	411.8(1)
23.30(2)	600	8.3689(5)	5.4851(4)	9.500(1)	116.34(3)	395.3(1)
3.95(2)	700	8.8434(5)	5.6145(3)	10.089(1)	115.47(3)	452.3(1)
5.60(2)	700	8.8075(5)	5.5946(3)	10.052(1)	115.33(3)	447.7(1)
9.30(2)	700	8.7292(5)	5.5571(3)	9.962(1)	115.36(3)	435.1(1)
13.90(2)	700	8.5361(5)	5.5516(3)	9.8479(1)	116.03(3)	421.2(1)
19.70(2)	700	8.4382(5)	5.5055(3)	9.7327(1)	115.78(3)	404.3(1)
25.57(2)	700	8.3384(5)	5.4734(4)	9.4677(1)	116.35(3)	389.9(1)

Table S2. Thermal EoS parameters derived from the fitting of *P-V-T* data to the BM3-HP=Third-order Birch-Murnaghan compressional EoS in combination with the Holland Powell thermal-pressure EoS

Composition	V_0 (Å^3)	K_{T0} (GPa)	$K_{T}'_0$	α_0 (10^{-5} K^{-1})	θ_E
Garnet ($Prp_{21}Alm_{47}Grs_{31}Sps_1$)	1566.05(25)	170(1)	3.74(22)		
	1566.05(25)	170(1)	3.82(14)	2.71(5)	450[a]
Omphacite ($Quad_{48}Jd_{45}Ae_7$)	423.48(24)	121(2)	3.90(35)		
	423.48(24)	121(3)	3.97(34)	3.73(20)	343[a]
Epidote ($Ca_{2.02}Fe_{0.75}Al_{2.32}Si_{0.16}[SiO_4][Si_2O_7]O(OH)$)	461.57(23)	122(1)	2.51(16)		
	461.57(23)	124(2)	2.04(15)	3.04(13)	626[b]

Reference: [a] Faccincani et al., 2021, [b] Gottschalk, 2004

Table S3. Thermal EoS parameters derived from the BM3-EoS of garnet, omphacite, and epidote in this study compared with previous studies.

	Composition	V_0 (Å^3)	K_{T0} (GPa)	$K_{T}'{}_0$	$(\partial K_T/\partial T)_P$ (GPa/K)	α_0 (10^{-5} K^{-1})		References
	$Prp_{21}Alm_{47}Grs_{31}Sps_1$	1566.05(25)	170(1)	3.82(14)		2.71(5)	XRD(SC)[a]	This study
	$Prp_{14}Alm_{62}Grs_{19}Adr_3Sps_2$	1564.9(1)	159.0(9)	5.0(2)	-0.010(4)	2.56(44)	XRD(SC)	(Xu et al., 2019)
	$Prp_{28}Alm_{38}Grs_{33}Sps_1$	1570.2(2)	162(1)	4.3(2)	-0.010(7)	3.53(35)	XRD(SC)	(Xu et al., 2019)
	$Prp_{68}Alm_{24}Gr_5Sp_1$		167(2)	4.4(1)	-0.0235(20)		BLS[b]	(Lu et al., 2013)
	$Prp_{26}Alm_{63}Grs_6Adr_5$	1542.43(11)	175(3)	3.7(7)			XRD(SC)	(Beyer et al., 2021)
	$Prp_2Alm_1Grs_{87}Adr_9$	1679.2	163.8(5)	3.9(2)			BLS	(Jiang et al., 2004)
Garnet	Prp_{100}	1499.9 (15)	170.7(30)	4.1^{fixed}	-0.024(13)	2.97(45)	XRD(ED)[c]	(Zou et al., 2012)
	Prp_{100}	1506.15(16)	163.7(1.7)	6.4		2.5(2)	XRD(SC)	(Milani et al., 2015)
	Alm_{100}	1533.52(10)	172.6(1.5)	5.8 (5)			XRD(SC)	(Milani et al. 2015)
	Alm_{100}	1531.05(7)	179(3)	4^{fixed}	-0.043(14)	2.6(5)	XRD(ED)	(Arimoto et al., 2015)
	Grs_{100}	1664.46(5)	166.57(17)	4.96 (7)		2.09(2)	XRD(SC)	(Milani et al., 2017)
	Sps_{100}	1564.96	172(4)	5.0(9)	-0.049(7)	2.46(54)	XRD(ED)	(Gréaux and Yamada, 2014)
	Adr_{100}	1754.05	158.0(1.5)	4^{fixed}	-0.020(3)	3.16(2)	XRD(PD)[d]	(Pavese et al., 2001)
	$Quad_{48}Jd_{45}Ae_7$	423.48(24)	121(3)	3.97(34)		3.73(20)	XRD(SC)	This study
	$Quad_{72}Jd_{28}$	424.7(7)	117(4)	6.9(12)	-0.026(5)	2.7(3)	XRD(PD)	(Nishihara et al., 2003)
	$Di_{70.5}Jd_{29.5}$	429(1)	122(3)s	4.6(5)		2.7(8)	XRD(SC)/BLS	(Hao et al., 2019)
Omphacite	$Quad_{57}Jd_{42}Ae_1$	422.3(1)	123.6(5)	4_{fixed}	-0.011(5)	2.8(3)	XRD(SC)	(Xu et al., 2019)
	$Quad_{53}Jd_{27}Ae_{20}$	426.0(2)	115(2)	4.9(4)	-0.009(6)	3.4(4)	XRD(SC)	(Xu et al., 2019)
	$Di_{51}Jd_{49}$	423.9(3)	116(2)	4.3(2)			XRD(SC)	(Zhang et al., 2016)
	$Di_{45}Jd_{55}$	421.43(4)	122(1)	5.1(3)			XRD(SC)	(Pandolfo et al., 2012a)
	$Di_{44}Jd_{56}$	421.04(7)	119(2)	5.7(6)		2.64(2)	XRD(SC)	(Pandolfo et al., 2012b)
	$Ca_{2.02}Fe_{0.75}Al_{2.32}Si_{0.16}(SiO_4)(Si_2O_7)O(OH)$	461.57(23)	124(2)	2.04(15)		3.04(13)	XRD(SC)	This study
	$Ca_2A1_2FeSi_3O_{12}(OH)$	459.9(3)	162(4)	4_{fixed}			XRD(PD)	(Holland et al., 1996)
Epidote	$Ca_{1.97}Fe_{0.84}\ Al_{2.15}(SiO_4)(Si_2O_7)O(OH)$	456.2(2)	133.1(7)	4_{fixed}	-0.004(1)	3.8(5)	XRD(SC)	(Li et al., 2020)
	$Ca_{1.85}Fe_{0.79}\ Al_{2.19}Ti_{0.05}Si_{3.03}O_{12}(OH)$	461.1(1)	115(2)	3.7(2)			XRD(SC)	(Qin et al., 2016)
	$Ca_{1.925}\ Fe_{0.745}Al_{2.265}Ti_{0.004}Si_{3.037}O_{12}(OH)$	458.8(1)	111(3)	7.6(7)		5.1(2)	XRD(PD)	(Gatta et al., 2011)
	$Ca_2Fe_{0.5}Al_{2.5}Si_3O_{12}(OH)$	463.8(6)	116(7)	7.8(8)			XRD(PD)	(Fan et al., 2014)

a: Single-crystal X-ray diffraction; b: Brillouin spectroscopy; c: Energy dispersive X-ray diffraction d: Powder X-ray diffraction

Quad: Ca-Mg-Fe pyroxene (Morimoto, 1988), Prp: Pyrope, Alm: Almandine, Grs: Grossular, Sps: Spessartine, Adr: Andradite, Jd: Jadeite, Ae: Aegirine, Di: Diopside.

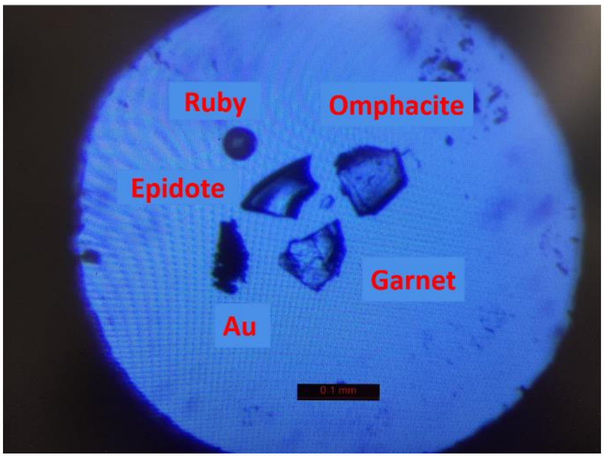

Figure S1. Representative sample chamber image showing garnet, omphacite, and epidote chips, together with Au and ruby sphere calibrant in Ne medium.

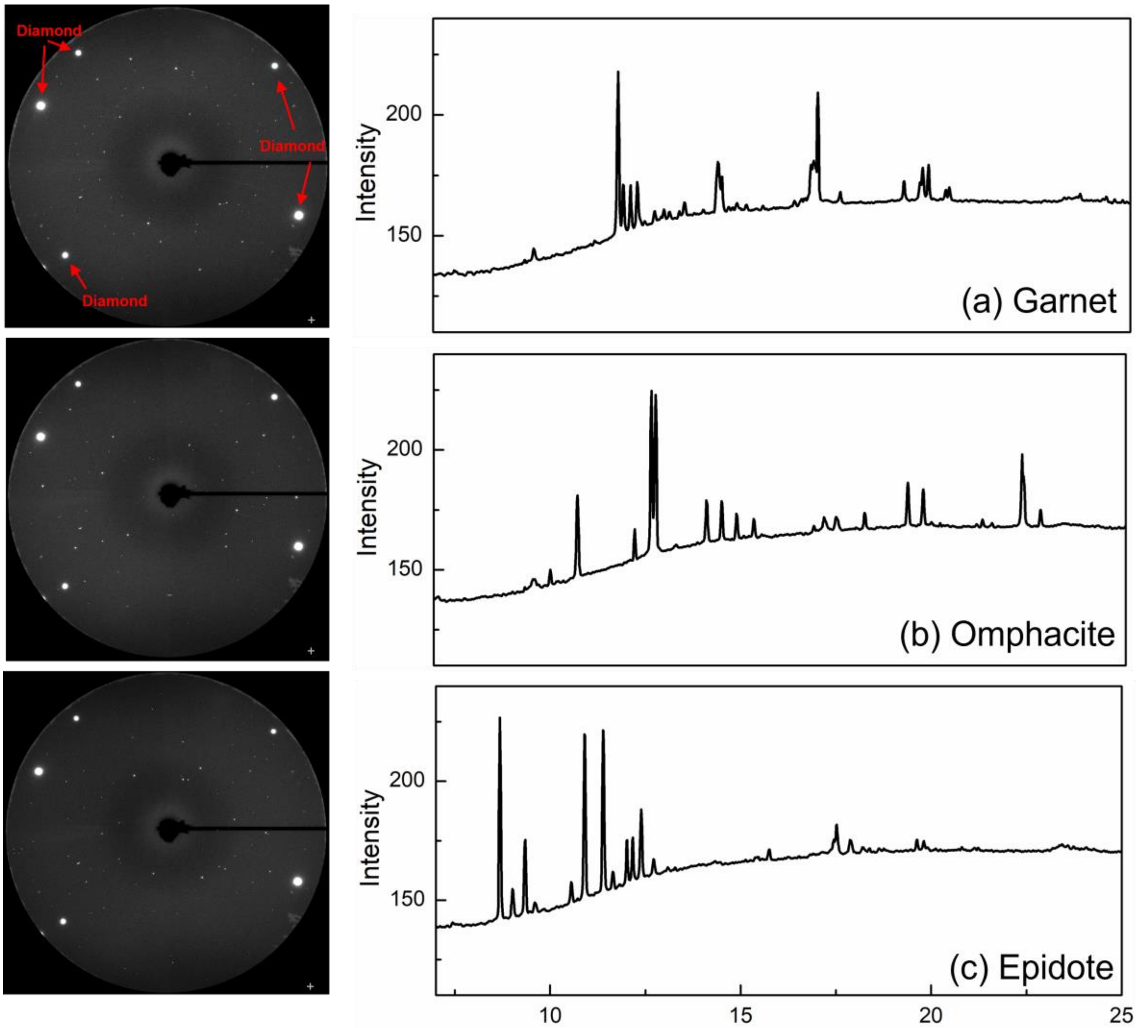

Figure S2. Representative single-crystal X-ray diffraction patterns of (a) garnet, (b) omphacite, (c) and epidote at 3.07 GPa and 600 K.

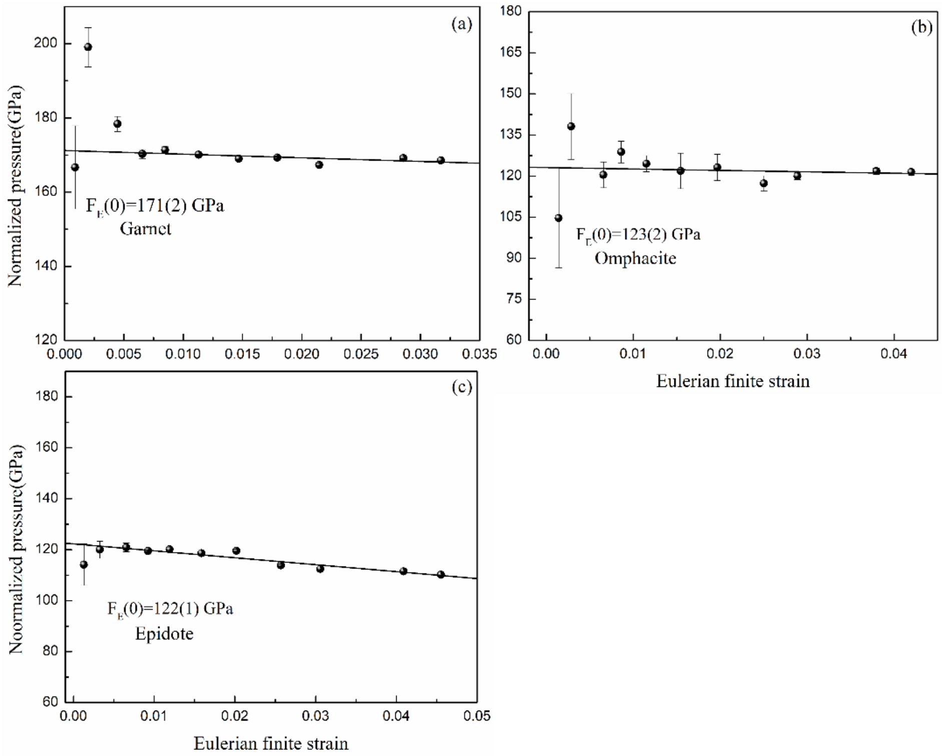

Figure S3. Eulerian finite stain-normalized pressure (F_E -f_E) plot of Garnet (a), Omphacite (b), and Epidote (c). The solid lines represent the linear fit through the data.

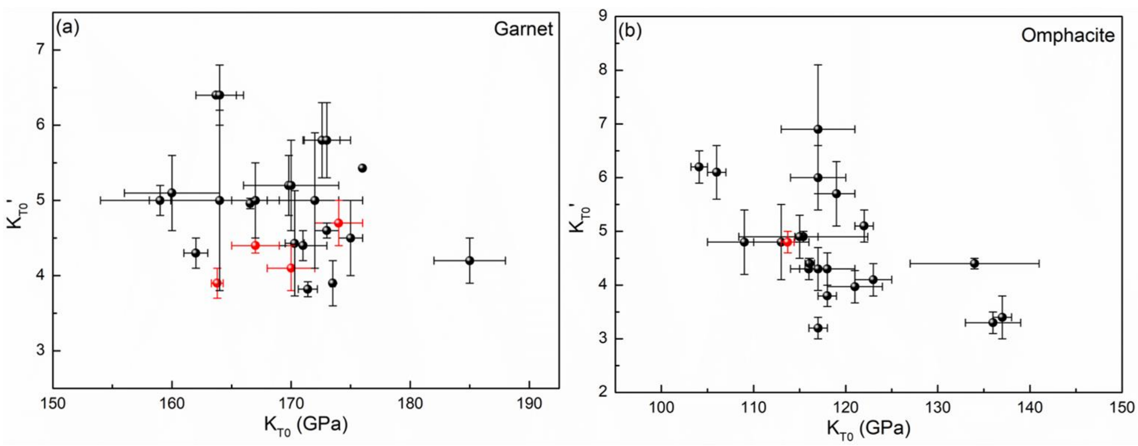

Figure S4. The isothermal bulk modulus (K_{T0}) and its pressure derivative (K_{T0}') plot of garnet (a) and omphacite (b). The red solid circles represent the results of Brillouin light scattering. The adiabatic bulk moduli (K_{S0}) obtained with BLS are converted to K_{T0} by the relationship K_{S0}= K_{T0} (1+$\alpha\gamma T$), where α is the thermal expansion, γ is the Grüneisen parameter, and T is the temperature.

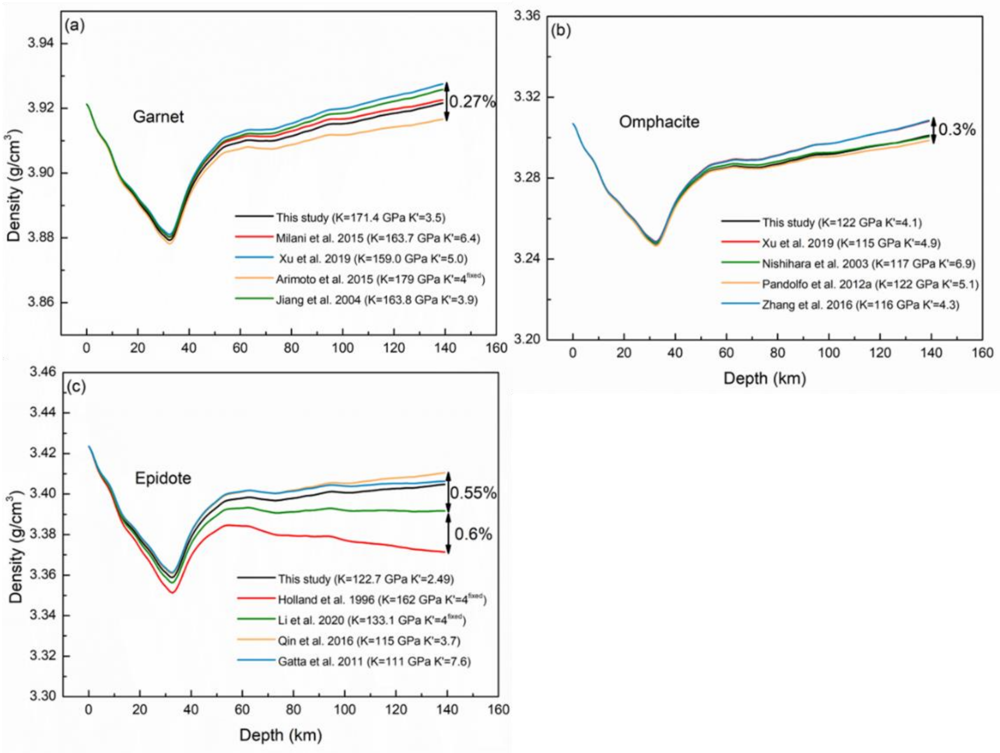

Figure S5. Density profiles of garnet (a), omphacite (b), and epidote (c) along with the Tibetan geothermal line. Different colored lines represent the calculated density profiles are derived from K_{T0} and K_{T0}'in different experiments, while other thermoelastic parameters are derived from this paper.

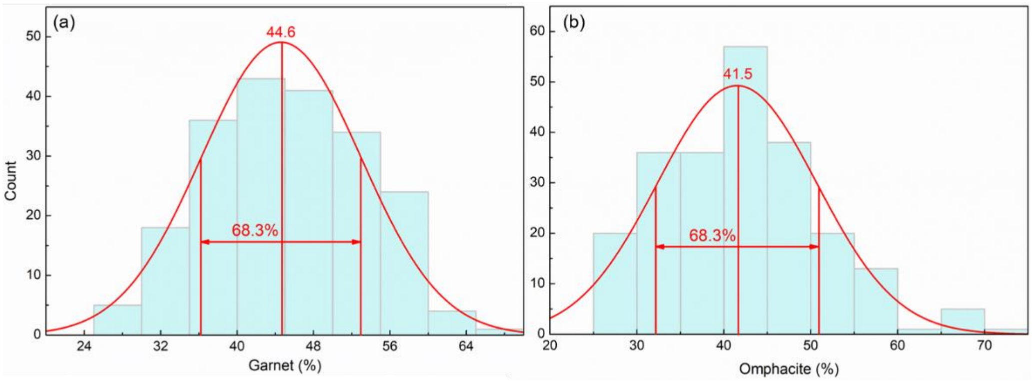

Figure S6. Normal distributions of garnet (a) and omphacite (b) content in eclogite from Tibet.

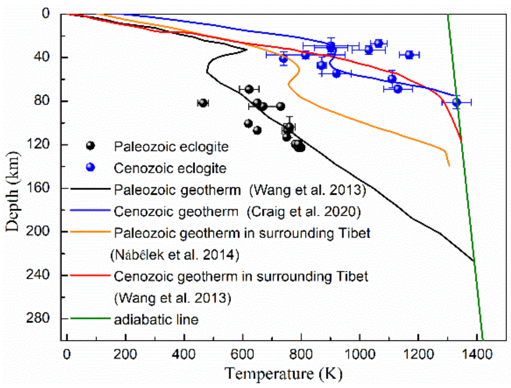

Figure S7. The geothermal lines of Tibet. The black line from Wang et al. (2013) represents the Paleozoic geotherm, which indicates relatively cold conditions. The delamination of the Neo-Tethyan slab breakoff accrues under such conditions. The orange line represents the geothermal line of surrounding Tibet during this period (Nábělek and Nábělek, 2014). The blue line represents the Cenozoic geotherm in Tibet (Craig et al., 2020), which indicates a relatively hot geotherm under the situation of convective removal. The red line represents the geothermal line of the surrounding Tibet in this situation (Wang et al., 2013). The green line is the adiabatic line. The black and blue solid circles correspond to the temperature and pressure conditions of exposed Tibetan eclogite in the Paleozoic and Cenozoic, respectively. The Paleozoic samples are referred from (Cheng et al., 2012, 2015; Dong et al., 2016, 2018; Huang et al., 2015; Li et al., 2017; Liu et al., 2019; Tang et al., 2020; Weller et al., 2016; Yang et al., 2019, 2014) and the Cenozoic samples are referred from (Chan et al., 2009; Corrie et al., 2010; Hacker, 2000).

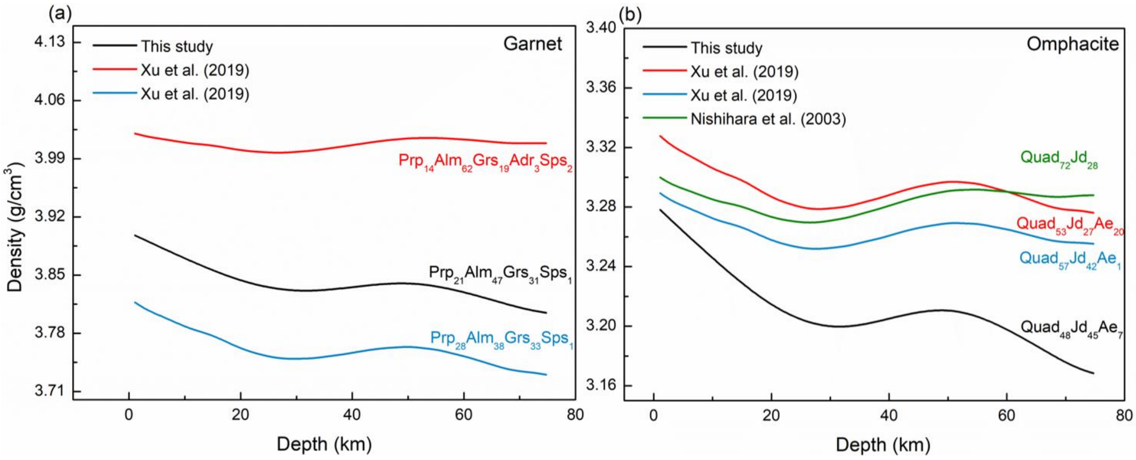

Figure S8. Density profiles of garnet (a) and omphacite (b) along the Cenozoic geothermal line. The garnets of $Prp_{14}Alm_{62}Grs_{19}Adr_3Sps_2$ and $Prp_{28}Alm_{38}Grs_{33}Sps_1$ are referred from Xu et al. (2019). The omphacites of $Quad_{53}Jd_{27}Ae_{20}$ and $Quad_{57}Jd_{42}Ae_1$ are from Xu et al. (2019) and $Quad_{72}Jd_{28}$ is from Nishihara et al. (2003).

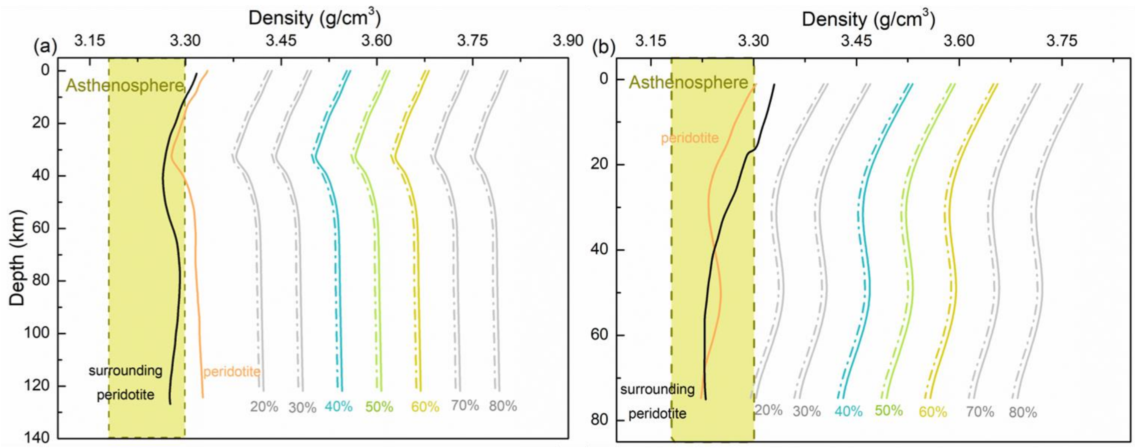

Figure S9. Density profiles of eclogite assemblages with and without epidote along the Paleozoic (a) and Cenozoic (b) geothermal lines. The solid line represents eclogite containing 5 vol. % epidote, while the dotted line indicates eclogite without epidote.

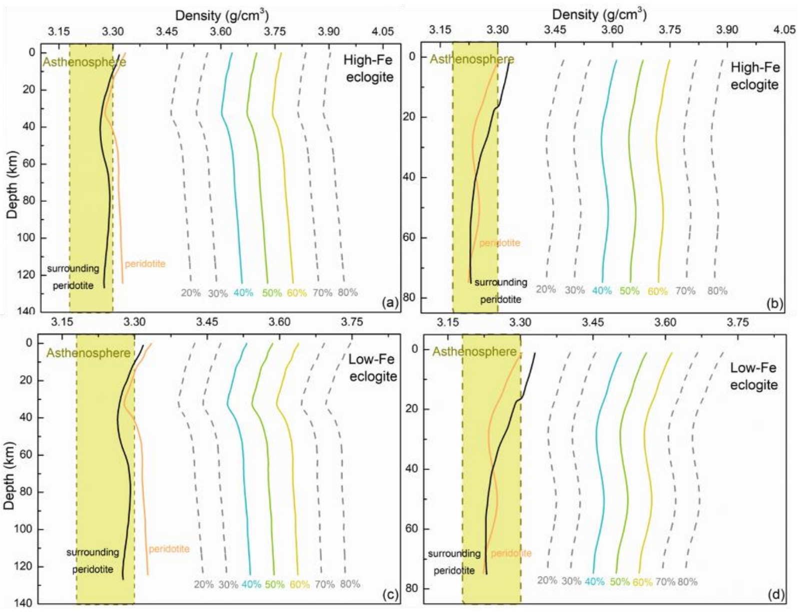

Figure S10. Density profiles of High-Fe and Low-Fe eclogite assemblages along the Paleozoic (a and c) and Cenozoic (b and d) geothermal lines. High-Fe eclogite is composed of $Prp_{14}Alm_{62}Grs_{19}Adr_{3}Sps_{2}$ and $Quad_{53}Jd_{27}Ae_{20}$, and Low-Fe eclogite is composed of $Prp_{28}Alm_{38}Grs_{33}Sps_{1}$ and $Quad_{57}Jd_{42}$ Ae_{1} (Xu et al., 2019).

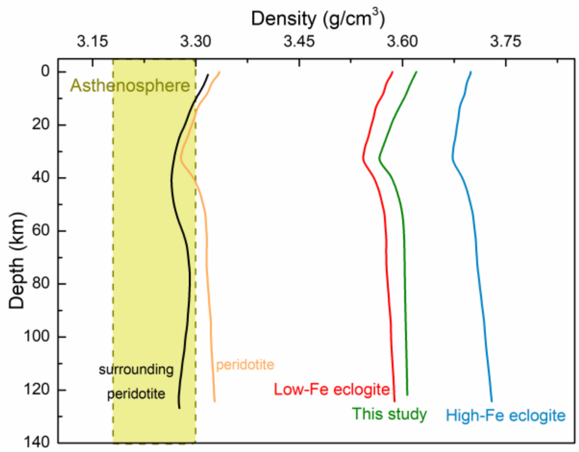

Figure S11. Density profiles of eclogite with different Fe contents with 50 vol. % garnet along the Paleozoic geothermal line.

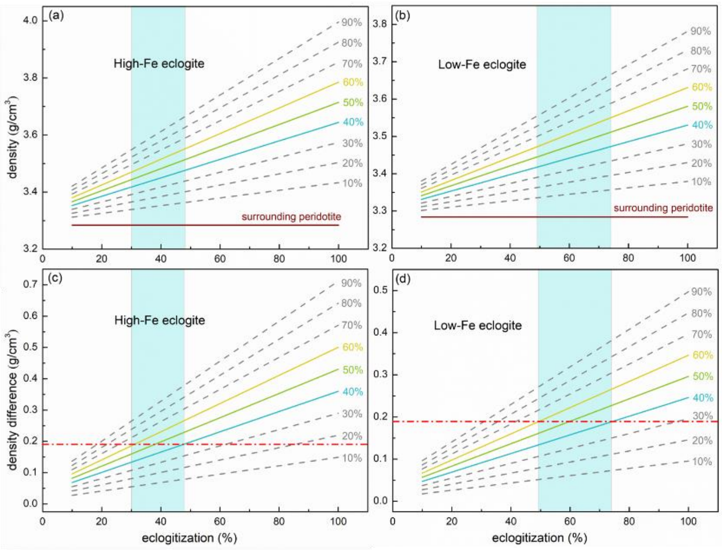

Figure S12. The effect of eclogitization on the density of subducted slab with high-Fe (a) and low-Fe (b) eclogite along the Paleozoic geothermal line. The rufous line represents the average density of the surrounding peridotite in this study. The blue shading indicates the possible degree of eclogitization. The density difference between high-Fe (c) and low-Fe (d) eclogite with different degrees of eclogitization and surrounding peridotite. The rufous line represents the average density of surrounding peridotite in this study. The blue shading indicates the possible degree of eclogitization.

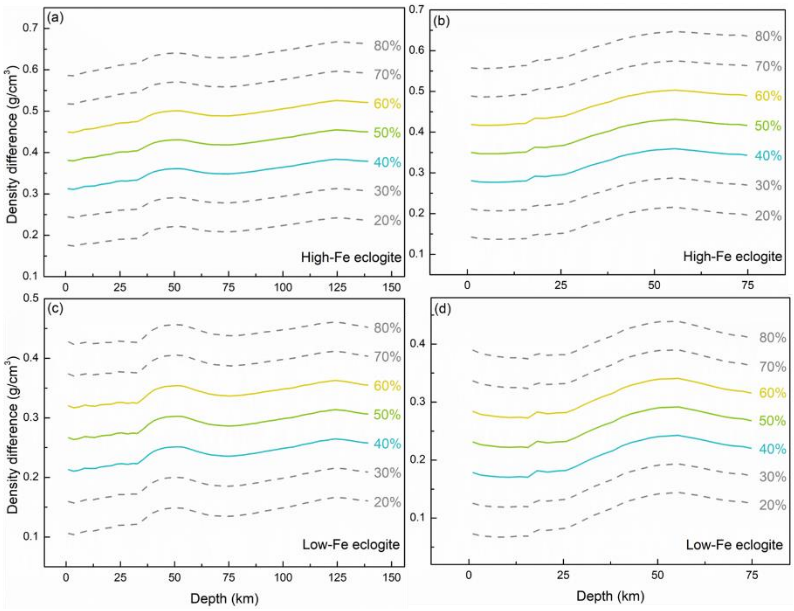

Figure S13. The density difference between High-Fe and Low-Fe eclogite assemblages and peridotite along the Paleozoic (a and c) and Cenozoic (b and d) geothermal lines, respectively.

References:

Arimoto, T., Gréaux, S., Irifune, T., Zhou, C. and Higo, Y.: Sound velocities of $Fe_3Al_2Si_3O_{12}$ almandine up to 19 GPa and 1700 K, Phys. Earth Planet. Inter., 246, 1–8, doi:10.1016/j.pepi.2015.06.004, 2015.

Beyer, C., Kurnosov, A. V., Ballaran, T. B. and Frost, D. J.: High-pressure and high-temperature single-crystal X-ray diffraction of complex garnet solid solutions up to 16 GPa and 823 K, Phys. Chem. Miner., 48(4), 17, doi:10.1007/s00269-021-01139-5, 2021.

Faccincani, L., Faccini, B., Casetta, F., Mazzucchelli, M., Nestola, F. and Coltorti, M.: EoS of mantle minerals coupled with composition and thermal state of the lithosphere: Inferring the density structure of peridotitic systems, Lithos, 404–405(September), 106483, doi:10.1016/j.lithos.2021.106483, 2021.

Fan, D., Xu, J., Wei, S., Chen, Z. and Xie, H.: In-situ high-pressure synchrotron X-ray diffraction of natural epidote, Chin. J. High

Press. Phys., 28, 257–261, doi:10.11858/gywlxb.2014.03.001, 2014.
Fei, Y.: Thermal Expansion, in Mineral Physics & Crystallography: A Handbook of Physical Constants, pp. 29–44., 1995.
Gatta, G. D., Merlini, M., Lee, Y. and Poli, S.: Behavior of epidote at high pressure and high temperature: a powder diffraction study up to 10 GPa and 1200 K, Phys. Chem. Miner., 38(6), 419–428, doi:10.1007/s00269-010-0415-y, 2011.
Gréaux, S. and Yamada, A.: P-V-T equation of state of $Mn_3Al_2Si_3O_{12}$ spessartine garnet, Phys. Chem. Miner., 41(2), 141–149, doi:10.1007/s00269-013-0632-2, 2014.
Gottschalk, M.: Thermodynamic Properties of Zoisite, Clinozoisite and Epidote, Rev. Mineral. Geochemistry, 56(1), 83–124, doi:10.2138/gsrmg.56.1.83, 2004.
Hao, M., Zhang, J. S., Pierotti, C. E., Ren, Z. and Zhang, D.: High-Pressure Single-Crystal Elasticity and Thermal Equation of State of Omphacite and Their Implications for the Seismic Properties of Eclogite in the Earth's Interior, J. Geophys. Res. Solid Earth, 124(3), 2368–2377, doi:10.1029/2018JB016964, 2019.
Holland, T. J. B., Redfern, S. A. T. and Pawley, A. R.: Volume behavior of hydrous minerals at high pressure and temperature; II, Compressibilities of lawsonite, zoisite, clinozoisite, and epidote, Am. Mineral., 81(3–4), 341–348, doi:10.2138/am-1996-3-408, 1996.
Jiang, F., Speziale, S. and Duffy, T. S.: Single-crystal elasticity of grossular- and almandine-rich garnets to 11 GPa by Brillouin scattering, J. Geophys. Res. Solid Earth, 109(B10), doi:10.1029/2004JB003081, 2004.
Li, B., Xu, J., Zhang, D., ZhilinYe, Huang, S., Fan, D., Zhou, W. and Xie, H.: Thermoelasticity and stability of natural epidote at high pressure and high temperature: Implications for water transport during cold slab subduction, Geosci. Front., (January), doi:10.1016/j.gsf.2020.05.022, 2020.
Lu, C., Mao, Z., Lin, J., Zhuravlev, K. K., Tkachev, S. N. and Prakapenka, V. B.: Elasticity of single-crystal iron-bearing pyrope up to 20GPa and 750K, Earth Planet. Sci. Lett., 361, 134–142, doi:10.1016/j.epsl.2012.11.041, 2013.
Milani, S., Nestola, F., Alvaro, M., Pasqual, D., Mazzucchelli, M. L., Domeneghetti, M. C. and Geiger, C. A.: Diamond–garnet geobarometry: The role of garnet compressibility and expansivity, Lithos, 227, 140–147, doi:10.1016/j.lithos.2015.03.017, 2015.
Milani, S., Angel, R. J., Scandolo, L., Mazzucchelli, M. L., Ballaran, T. B., Klemme, S., Domeneghetti, M. C., Miletich, R., Scheidl, K. S., Derzsi, M., Tokár, K., Prencipe, M., Alvaro, M. and Nestola, F.: Thermo-elastic behavior of grossular garnet at high pressures and temperatures, Am. Mineral., 102(4), 851–859, doi:10.2138/am-2017-5855, 2017.
Morimoto, N.: Nomenclature of Pyroxenes, Mineral. Petrol., 39(1), 55–76, doi:10.1007/BF01226262, 1988.
Nishihara, Y., Takahashi, E., Matsukage, K. and Kikegawa, T.: Thermal equation of state of omphacite, Am. Mineral., 88(1), 80–86, doi:10.2138/am-2003-0110, 2003.
Pandolfo, F., Nestola, F., Cámara, F. and Domeneghetti, M. C.: High-pressure behavior of space group P2/n omphacite, Am. Mineral., 97(2–3), 407–414, doi:10.2138/am.2012.3928, 2012a.
Pandolfo, F., Nestola, F., Cámara, F. and Domeneghetti, M. C.: New thermoelastic parameters of natural C2/c omphacite, Phys. Chem. Miner., 39(4), 295–304, doi:10.1007/s00269-012-0484-1, 2012b.
Pavese, A., Diella, V., Pischedda, V., Merli, M., Bocchio, R. and Mezouar, M.: Pressure-volume-temperature equation of state of andradite and grossular, by high-pressure and -temperature powder diffraction, Phys. Chem. Miner., 28(4), 242–248, doi:10.1007/s002690000144, 2001.
Qin, F., Wu, X., Wang, Y., Fan, D., Qin, S., Yang, K., Townsend, J. P. and Jacobsen, S. D.: High-pressure behavior of natural single-crystal epidote and clinozoisite up to 40 GPa, Phys. Chem. Miner., 43(9), 649–659, doi:10.1007/s00269-016-0824-7, 2016.
Xu, J., Zhang, D., Fan, D., Dera, P. K., Shi, F. and Zhou, W.: Thermoelastic Properties of Eclogitic Garnets and Omphacites: Implications for Deep Subduction of Oceanic Crust and Density Anomalies in the Upper Mantle, Geophys. Res. Lett., 46(1), 179–188, doi:10.1029/2018GL081170, 2019.
Zhang, D., Hu, Y. and Dera, P. K.: Compressional behavior of omphacite to 47 GPa, Phys. Chem. Miner., 43(10), 707–715, doi:10.1007/s00269-016-0827-4, 2016.
Zou, Y., Gréaux, S., Irifune, T., Whitaker, M. L., Shinmei, T. and Higo, Y.: Thermal equation of state of $Mg_3Al_2Si_3O_{12}$ pyrope garnet up to 19 GPa and 1700 K, Phys. Chem. Miner., 39(7), 589–598, doi:10.1007/s00269-012-0514-z, 2012